Boundary-Layer Meteorol (2013) 147:21–39
DOI 10.1007/s10546-012-9772-z

ARTICLE

Flume Experiments on Turbulent Flows Across Gaps of Permeable and Impermeable Boundaries

S. Fontan · G. G. Katul · D. Poggi · C. Manes · L. Ridolfi

Received: 25 January 2012 / Accepted: 18 September 2012 / Published online: 17 October 2012

Abstract Laser Doppler anemometery and laser-induced fluorescence techniques were used to explore the spatial structure of the flow within and above finite cavities created within porous and solid media. The cavities within these two configurations were identical in size and were intended to mimic flow disturbances created by finite gaps and forest clearing. Because flows over permeable boundaries differ from their solid counterparts, the study here addresses how these differences in boundary conditions produce differences in, (i) bulk flow properties including the mean vorticity within and adjacent to the gaps, (ii) second-order statistics such as the standard deviations and turbulent stresses, (iii) the relative importance of advective to turbulent stress terms across various regions within and above the gaps, and (iv) the local imbalance between ejections and sweeps and momentum transport efficiencies of updrafts and downdrafts. Both configurations exhibited a primary recirculation zone of comparable dimensions inside the gap. The mean vorticity spawned at the upstream corner of the gap was more intense for the solid configuration when compared to its porous counterpart. The free-shear layer spawned from the upstream corner-edge deeper into the gap for the porous configuration. The momentum flux at the interface within and above the gap was enhanced by a factor of 1.5–2.0 over its upstream value, and this enhancement zone was much broader in size for the porous configuration. For the turbulent transport terms in the longitudinal and vertical mean momentum balances, these transport terms were significant

S. Fontan (✉) · D. Poggi · L. Ridolfi
Dipartimento di Ingegneria dell'Ambiente, del Territorio e delle Infrastrutture,
Politecnico di Torino, Torino, Italy
e-mail: stefano.fontan@polito.it

G. G. Katul
Nicholas School of the Environment, Duke University, Durham, NC, USA

G. G. Katul
Department of Civil and Environmental Engineering, Duke University, Durham, NC, USA

C. Manes
Department of Engineering and the Environment, Energy and Climate Change Research Group,
University of Southampton, Southampton SO17 1RJ, UK

inside the gap for both boundary configurations when compared to their upstream counterpart. The effectiveness of using incomplete cumulant expansion methods to describe the momentum transport efficiencies, and the relative contributions of ejections and sweeps to turbulent stresses, especially in this zone, were also demonstrated. The flatness factor for both velocity components, often used as a measure of intermittency, was highest in the vicinity of the upstream corner in both configurations. However, immediately following the downstream corner, the flatness factor remained large for the porous configuration, in contrast to its solid configuration counterpart.

Keywords Backfacing step flow · Conditional sampling · Flow within cavities · Forest gaps · Recirculation zone

1 Introduction

Studies on flow disturbances created by gaps and clearings within forested ecosystems are receiving significant attention given their implications on a plethora of processes such as seed and pollen dispersal by wind, aerosol deposition onto canopies, spatial aggregation of momentum, mass, and energy exchange rates within fragmented landscapes, bulk drag estimates for large-scale models, among others (Klaassen 1992; Veen et al. 1996; Albertson and Parlange 1999; Laurence 2004; Cassiani et al. 2008; Detto et al. 2008). Mean and turbulent flow properties near forested edges have been reported in a number of field studies though their spatial sampling remains rather restricted to few tower locations and levels (Irvine et al. 1996; Thomas and Wilson 1999; Detto et al. 2008). In the last decade, large-eddy simulations (LES) have been used to explore the effects of forest edges on flow disturbances at unprecedented resolutions (Yang et al. 2006a,b; Cassiani et al. 2008; Dupont and Brunet 2008; Schlegel et al. 2012). For flows traversing a clearing and entering into a dense forested patch, these LES studies reveal a number of common features (Dupont and Brunet 2008; Cassiani et al. 2008) including, (i) the formation of an adverse pressure gradient just upwind from the edge that initiates a deceleration in the longitudinal velocity component, (ii) an adjustment region inside the canopy in which the longitudinal velocity further reduces due to the presence of canopy drag elements resulting in an upward vertical motion from the canopy volume as schematically shown in Fig. 1. Turbulent intensity also decreases within the canopy due to the presence of small wakes that enhance the turbulent kinetic energy (TKE) dissipation rate (Belcher et al. 2003). Perhaps more significant is the occurrence of a so-called enhanced gust zone near the canopy top at the clearing-forest interface characterized by high intermittency and non-Gaussian statistics (see Fig. 1). Interest in this zone is now proliferating given its implications to wind-induced tree damage (Dupont and Brunet 2008). On the other hand, flows traversing a dense forested canopy into a gap or a clearing share some similarities with back-facing step (BFS) flows known to exhibit separation and re-attachment zones (Detto et al. 2008; Cassiani et al. 2008). In a conventional BFS set-up, as the flow traverses into a drop, the separation region is spawned by the sharp corner of the drop as shown in Fig. 1. Following this separation point, shedding of vortices occur due to the discontinuity imposed on the velocity at the corner interface (Simpson 1989; Spazzini et al. 2001). A primary recirculation region is then established below the separated layer along with an occasional secondary separation region near the ground adjacent to the corner. The vortex structure in the primary separated layer generally resembles mixing-free shear layers as shown in Fig. 1. Following this separation zone, a re-attachment zone is established and after some downstream distance, the flow re-equilibrates with the new surface. This BFS

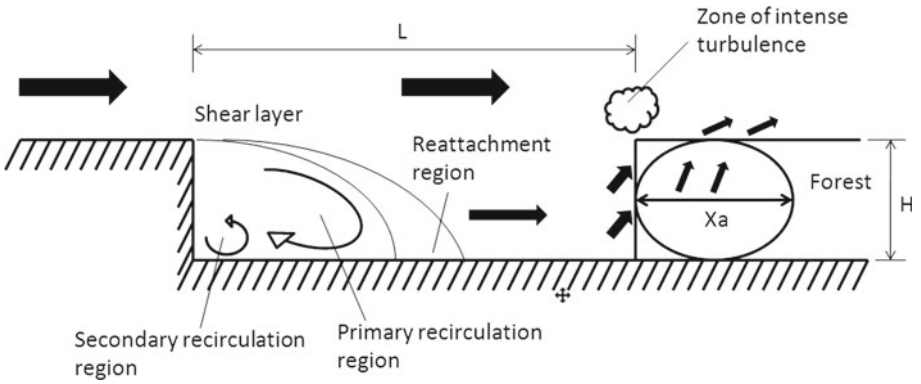

Fig. 1 The topology of turbulence for a back-facing step flow (*left*) and a zone of upward motion and intense turbulence as the flow traverses into a densely forested canopy from a gap (*right*)

mean flow 'topology' may be dramatically altered in two ways within clearings and gaps. In small and mid-sized gaps, the size of the primary separation region and the re-attachment zone may not be allowed to freely establish. Moreover, dense forested canopies do not impose the same no-slip constraints on the flow as in a BFS and their permeability allows for some pressure relaxation and adjustments that are absent in solid boundaries. In fact, turbulent flows over permeable boundaries differ from their solid counterparts, especially with regards to the type of coherent structures near the boundary (Raupach et al. 1996; Finnigan 2000; Manes et al. 2011). It is this latter point, with its implications to flows in gaps and clearings, that motivated our study. How a porous medium alters the BFS vortical topology and any modifications arising due to finite gap dimensions is explored here using detailed flume experiments. The emphasis is on addressing how differences in these two boundary conditions produce differences in, (i) bulk flow properties including the mean vorticity within and adjacent to the gaps, (ii) second-order statistics such as the standard deviations and turbulent stresses, (iii) the relative importance of advective to turbulent stress terms across various regions within and above the gaps, and (iv) the local imbalance between ejections and sweeps and momentum transport efficiencies of updrafts and downdrafts.

2 Laboratory Experiments

The experiments were conducted in a large non-tilting re-circulating rectangular flume at the *G. Bidone Hydraulics Laboratory* in Politecnico di Torino, Turin, Italy. The flume is 18 m long and 0.9 m wide built with glass side walls to permit optical access. A steady water depth of $h = 0.4$ m at the upstream end was maintained throughout the experiments. For modelling a forest, the flume bottom was covered with a mattress block made of Polyester foam (PPI30) having a thickness $H = h/4$, a filament thickness of 0.11 mm, a mean pore size of 1.5 mm (Manes et al. 2011), and a porosity that is approximately homogeneous and isotropic. These pore configurations correspond to an effective leaf area index (LAI) equivalent to about 3.5 $m^2\ m^{-2}$, which is common to many forested canopies (Detto et al. 2008; Cassiani et al. 2008; Schlegel et al. 2012). A gap was created by splitting the mattress block into two parts and then separating them apart by an adjustable distance L whose value is discussed later. Two mattress porosity values were considered as end-members for the boundary

conditions. The first is a 97 % porosity mattress, which was deemed to be sufficiently large so that finite porosity effects can be ignored. The second is zero, which is the extremum condition representing a non-porous or 'solid configuration'. This so-called solid configuration was constructed by covering the two mattress blocks constituting the gap with a smooth stainless steel sheet.

2.1 Visualizations

Dye laser visualization (DLV) runs were carried out to first identify a gap size and Reynolds number configuration that is dynamically rich for exploring the mean momentum balance, the mean vorticity, and the momentum transfer properties, and yet relevant to forest gap dynamics in such a way as to analyze small discontinuities until the infinity case. The DLV is based on the planar laser induced florecence (LIF) technique, which is employed here to measure the local instantaneous dye concentration in the flow. The DLV runs were conducted by releasing Fluorescein and Rhodamine 6G upstream of the gap. When excited by a laser, Fluorescein and Rhodamine 6G emit a metallic green and a bright red light, respectively, that can be imaged. The details of the LIF instrumentation and data processing are discussed elsewhere (Poggi et al. 2006, 2011). The gap size to be identified by the DLV runs is a compromise between very small gaps that dictate the size of the vortical structure and very large gaps that have been extensively studied as isolated forest edges. In a very small-gap set-up, as the flow transverses over the gap, the small gap size permits limited eddy penetration thereby dictating the primary size of the recirculating zone. On the other hand, flow over very large gaps approach a quasi BFS immediately after the drop and then re-equilibrate following the reattachment region. The newly equilibrated flow will encounter the downstream end face of the gap, experience a disturbance, and re-adjust accordingly. This latter adjustment has received theoretical and experimental attention as earlier noted (Belcher et al. 2003; Yang et al. 2006a,b; Cassiani et al. 2008; Seraphin and Guyenne 2008) and is not the main focus here. Rather, the focus here is on a configuration that allows a separated shear layer to be initiated and developed but with a minimal re-attachment zone. This case is dynamically interesting because the adjustment phase immediately following the re-attachment phase encounters the downstream gap face. An initial DLV exploration was conducted by placing four laser sources that project a plane of light along the central axis of the channel (0.6 m along the longitudinal axis and 0.4 mm thick) and four cameras positioned in such a way so that their combined view captures the entire light plane at 25 frames s^{-1}. The injection tubes (upstream) and the mattress used for the porous case are shown in Fig. 2a. The positioning of the two mattress blocks, the injection tubes, and the laser source are also presented schematically in Fig. 2b. The intent of these DLV runs was to explore three main characteristic parameters on the separation and re-attachment within the gap: porosity, gap dimension, and Reynolds number effects. The DLV runs were conducted for a combination of two porosity values, two Reynolds number values, and five gap-size values as shown in Fig. 3a. In presenting the DLV results in Fig. 3a, the width-to-height ratio $L/H = GR$ (Gap Ratio) is varied by varying L, keeping H and h constant. When $GR = 0.5$, the DLV suggests that the primary vortex size appears to be dictated by L. If GR is between 1 and 2, the separated shear layer initiated from the upstream edge forms due to vortex shedding at the corner but is prematurely censored at the downstream end of the gap. However, for $GR = 3$, the separated shear layer appears to fill the gap just prior to the formation of a typical BFS re-attachment zone. When $GR \geq 5$, the shear layer re-attaches along the gap floor before being disturbed by the downstream side of the gap (Ashcroft and Zhang 2008). In this case, the effects of the gap walls share many analogies with configurations that are well studied in the literature as earlier noted (Seraphin

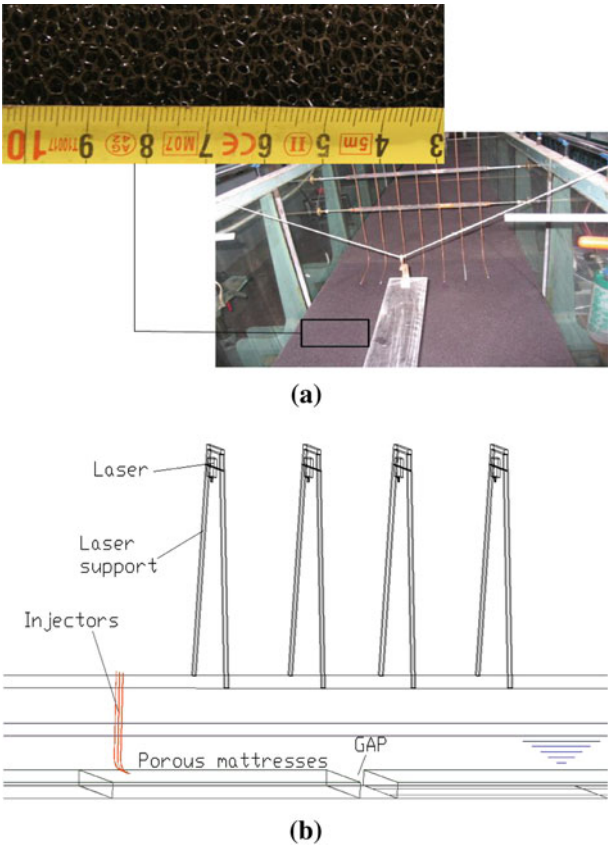

Fig. 2 Laboratory set-up for the DLV runs showing the positioning of the cameras, the dye injection tubes, the mattress foam representing the porous media, and a schematic of the overall setup. **a** Polyester foam and dye injectors. **b** Dye injection and visualization set-up. The mean flow is from *left to right*

and Guyenne 2008; Dupont and Brunet 2008; Cassiani et al. 2008). Hence, based on these DLV results, $GR = 3$ was selected for exploring the effects of porous and solid boundaries on the flow statistics. This GR configuration is also commensurate with a forest clearing field study in which the gap length was 60 m and the canopy height was 30 m (i.e. $GR = 2$) described elsewhere (Schlegel et al. 2012).

2.2 Laser Doppler Anemometer

In describing the flow statistics, meteorological notation is adopted with x and z defining the longitudinal and vertical coordinates ($z = 0$ being the channel bed), $\overline{U}$ and $\overline{W}$ are the mean longitudinal and vertical velocity components, respectively, u' and w' are instantaneous turbulent fluctuations from $\overline{U}$ and $\overline{W}$, respectively. Throughout, primed quantities indicate turbulent excursions from the mean state indicated by the overbar. The instantaneous $u = \overline{U} + u'$ and $w = \overline{W} + w'$ time series were acquired using laser Doppler anemometry (LDA) operated in forward scattering mode. The LDA system, data acquisition, and processing routines are discussed elsewhere (Poggi et al. 2002). Laser acquisition parameters were adjusted for every point to cover all the expected range in velocity fluctuations. The

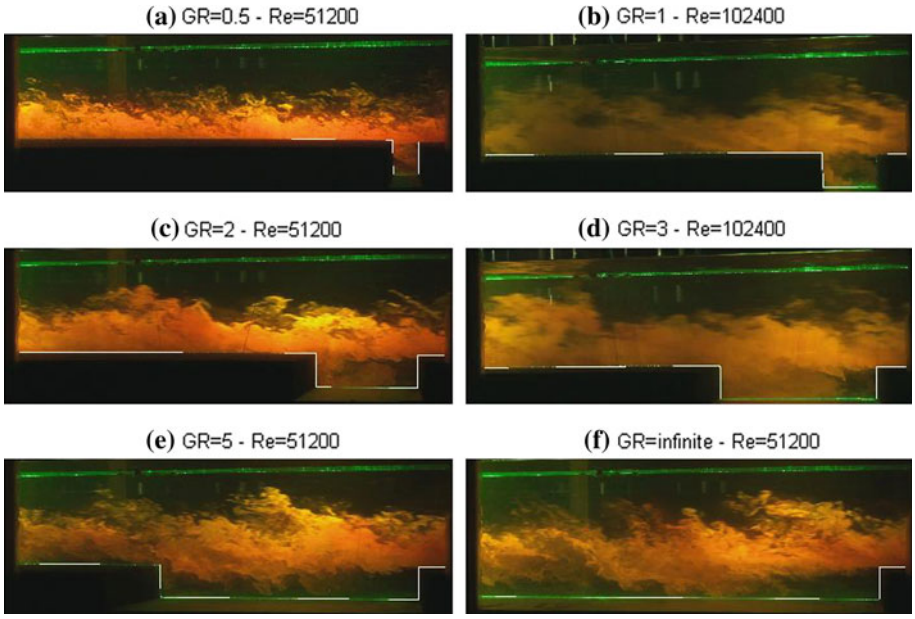

Fig. 3 Laser-induced fluorescence (LIF) dye visualization runs for various GR configurations and bulk Reynolds numbers Re_b (based on upstream depth-averaged velocity and h)

main acquisition parameters to be adjusted are the signal gain, the voltage to the photomultiplier, and an estimate of the mean velocity and its root-mean-squared fluctuation. The LDA inclination angle configuration employed here results in the nearest velocity sampling point to be 0.015 m above the mattress. Measured velocity profiles were sampled every 0.01 m throughout the water level. The horizontal spatial sampling resolution was chosen in such a way as to optimally describe gradients in the flow within the gap. Data were collected as five series of 2 min per sampling location per velocity component. The sampling rate is a function of the velocity component and varied from 7,000 to 40,000 samples for every series (roughly coinciding with sampling frequencies between 60 and 350 Hz). All the acquired series were combined and used to compute first-, second-, and third-order moments of the flow field, the mean vorticity, the mean advective and turbulent transport terms, momentum transport efficiencies in updrafts and downdrafts, and ejection-sweep properties at all sampled locations and for the configurations identified by the DLV runs. The measurement locations as well as the mean velocity are presented in Fig. 4 as 'quiver' plots. Quiver plots assign the base of each arrow to the sampling location, while the angle and length of each arrow indicate the direction and magnitude of the mean velocity vector, respectively. It is evident from Fig. 4 that the primary recirculation region fills the gap as expected from the DLV runs, and the re-attachment zone is almost confined to the downstream gap face. Table 1 shows the pertinent flow variables and dimensionless numbers for the solid and porous configurations. In these experiments, the friction velocity (u_*) was determined by extrapolating the Reynolds stress profile ($\overline{u'w'}(z)$) to the surface using measurements at a location undisturbed by the gap (about 0.4 m upstream of it). For the porous mattress, u_* was determined by fitting $\overline{U}$ to the logarithmic mean velocity profile, and the value estimated was comparable (i.e. within 10 %) to the u_* value inferred from linearly extrapolating the turbulent stress profile to $z = 0$. For the solid boundary, the limited sampling points near the surface prohibited the use of the

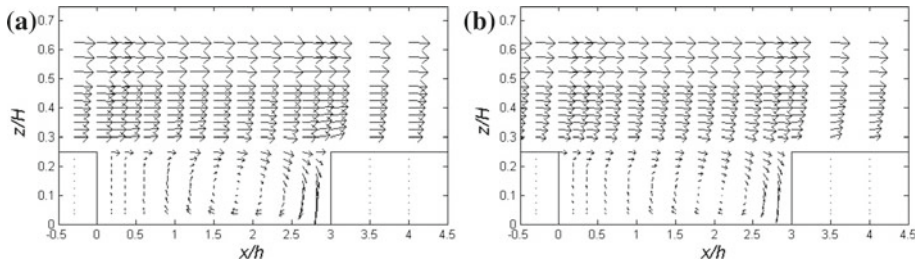

Fig. 4 The mean velocity vectors and their measurement locations with respect to the gap for the solid (**a**) and porous (**b**) boundaries

Table 1 The main flow variables and dimensionless numbers for the solid and porous boundaries, where Q is the bulk steady flow rate, h is the water depth, u_* is the inferred friction velocity from extrapolating the Reynolds stress profile, z_o is the aerodynamic roughness length of the porous boundary estimated from the upstream mean velocity profiles, $\delta = 5u_*/\nu$ is the thickness of the viscous sublayer for the solid boundary, ν is the kinematic viscosity, Re_b is the bulk flow Reynolds number, Re_r is a roughness Reynolds number, Fr is the Froude number showing that the flow maintained a subcritical state throughout, and g is the gravitational acceleration

Name	Solid configuration	Porous configuration	Typical values
Q ($m^3\,s^{-1}$)	0.1	0.1	–
h (m)	0.4	0.4	–
u_* $m\,s^{-1}$	0.045	0.046	–
δ or z_0 (m)	1.2×10^{-4}	1.7×10^{-3}	–
$Re_b = \frac{\overline{U}h}{\nu}$	102,400	102,400	–
$Re_r = \frac{u_* z_0}{\nu}$	4.8	70.1	–
$Fr = \frac{\overline{U}}{\sqrt{gh}}$	0.14	0.14	–
σ/u_*	–	–	3.3
σ_u/u_*	–	–	2.7
σ_w/u_*	–	–	1.1

logarithmic mean velocity profile to determine any roughness parameter. Hence, for the solid case, it was assumed that the flow is smooth with a viscous sublayer thickness estimated by $\delta = 5u_*/\nu$ (Pope 2000), where ν is the kinematic viscosity of water. Based on these estimates, the aerodynamic roughness length (z_o) for the porous boundary was one order of magnitude larger than δ.

3 Results and Discussion

The main goal of our study was to explore how differences in porous and solid boundaries produce differences in, (i) bulk flow properties within and adjacent to the gap, including any differences in the spatial structure of the mean vorticity, (ii) the relative importance of advective and turbulent transport terms in the mean longitudinal and vertical momentum balances for various regions across and within the gap, and (iii) the local imbalance between ejections and sweeps contribution to the momentum flux as well as the transport efficiencies

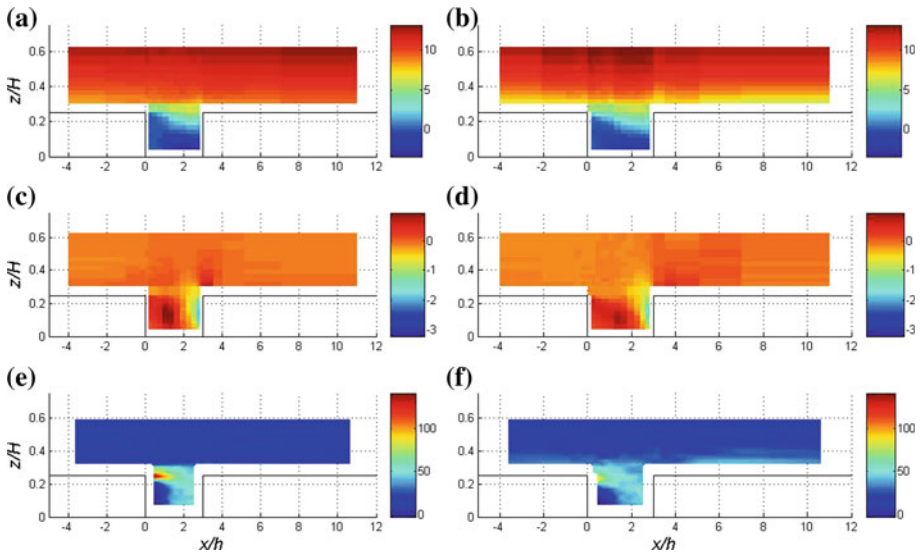

Fig. 5 The spatial variation of the normalized mean longitudinal ($\overline{U}/u_*$) and vertical ($\overline{W}/u_*$) velocities, and mean vorticity ($\omega_y(h/u_*)$) $= (h/u_*)(\partial\overline{U}/\partial z - \partial\overline{W}/\partial x)$ for the solid (*left*) and porous (*right*) configurations. **a, b** $\overline{U}/u_*$, **c, d** $\overline{W}/u_*$, **e, f** $\omega_y h/u_*$

of updrafts and downdrafts. Hence, Sect. 3 is structured to address these goals. Because the LDA flow measurements are used to evaluate the spatial variations in the mean velocity, mean vorticity, and advective terms in the mean longitudinal and vertical momentum balances, the estimation of the spatial gradients must be considered given the unavoidable measurement errors. While various approaches are available to interpolate and compute spatial gradients for noisy data, the approach followed here is intended to correct the time-averaged $\overline{U}$ and $\overline{W}$ so as to ensure that the mean fluid continuity equation is satisfied. These corrections are derived and discussed in the Appendix. When presenting the effects of the boundary on the flow statistics, u_* and h values given in Table 1 are used as normalizing variables for all velocity and length scales, respectively. The data are graphically presented as colour maps, where the colour intensity is proportional to the quantity being analyzed to emphasize variability across different regions within the flow domain. For convenience, GF_{U} and GF_{D} refer to the upstream and downstream gap faces, respectively.

3.1 Mean Velocity and Vorticity

Figure 5 show the measured normalized mean velocity components and the mean vorticity for the solid and porous configurations. The $\overline{U}$ well above the gap with solid boundaries appears to be insensitive to the presence of the gap (i.e. exhibiting a quasi planar-homogeneous behaviour), which is not the case for the porous boundary. For the latter, there is a 'speed-up' zone in $\overline{U}$ in the upper layers situated immediately above the gap. The measurements inside the gap show a rapid decrease in $\overline{U}$ for both solid and porous configurations as expected. Within the gap, both configurations also show the onset of a quasi-free shear layer initiated at the upstream corner point of GF_{U}, characterized by $\overline{U}/u_* \approx 3$. The $\overline{U}/u_* = 3$ is remarkably consistent with free-shear mixing layers and has been reported in numerous dense canopy flow experiments near the canopy top (Raupach et al. 1996; Katul et al. 1998;

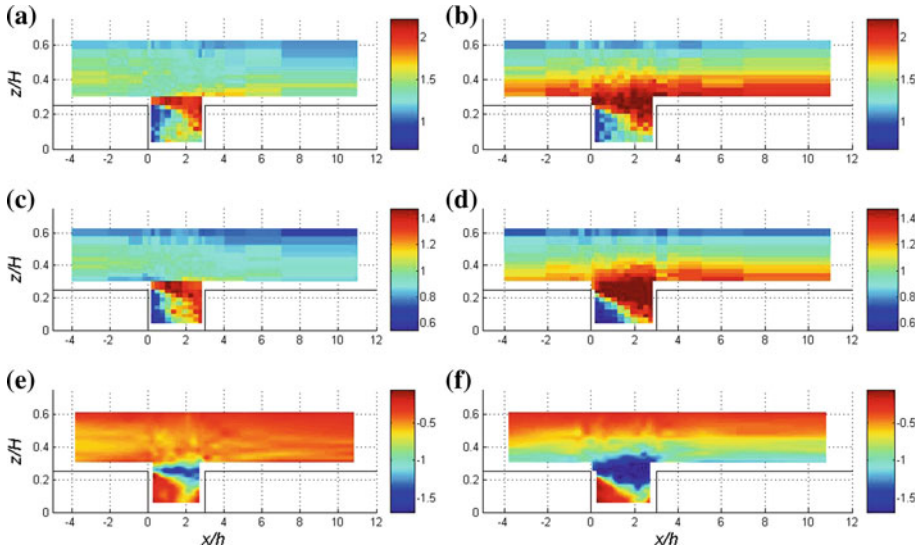

Fig. 6 The spatial variations of the normalized velocity standard deviations σ_u/u_* (*top*), σ_w/u_* (*middle*) and the normalized Reynolds stress $\overline{u'w'}/(u_*^2)$ (*bottom*) for the solid (*left*) and porous (*right*) configurations. **a, b** σ_u/u_*, **c, d** σ_w/u_*, **e, f** $\overline{u'w'}/(u_*^2)$

Finnigan 2000; Cava et al. 2006). For the porous configuration, this free-shear layer appears more space filling (i.e. the zone delineated by $\overline{U}/u_* \approx 3$ is commensurate with the gap size), again pointing out to the effects of the boundary on the mean flow structure within the gap. Both configurations exhibit a primary recirculation zone of comparable dimensions inside the gap, which was already noted in Fig. 4. For $\overline{W}$, the pronounced influences of the gap appear to be concentrated in two regions. The first is within the primary re-circulation zone with the expected downward mean flow induced by the GF_D and the concomitant upward mean flow region distributed from the GF_U and extending to the centre of the gap. The second region is the adjustment zone immediately after GF_D. In this zone, $\overline{W}$ is positive over a wider distance for the porous boundary, consistent with forest edge studies (Belcher et al. 2003; Dupont and Brunet 2008; Cassiani et al. 2008). Over the solid boundary, the positive $\overline{W}$ is large but narrowly confined to the immediate vicinity downstream of GF_D. The most striking difference introduced by the surface cover is the spawning of the mean vorticity ω_y. It is clear that over the solid boundary, the spawning of ω_y at GF_U is co-located with the upstream corner of the gap, consistent with BFS type flows (as expected). For the porous case, the spawning of ω_y is apparently more spatially diffuse presumably due to, (i) the lack of a sharp corner edge, and (ii) finite velocities in the porous matrix. Naturally, the large normalized $|\omega_y|(>1)$ delineates the free-shear interface within and immediately above the gap and is embedded within the zone for which $\overline{U}/u_* \approx 3$. Next, we explore how the generation and dissipation of ω_y affect the spatial variability of the velocity variances and turbulent stresses.

3.2 Velocity Standard Deviations and Reynolds Stresses

Figure 6 show the normalized longitudinal σ_u/u_* and vertical σ_w/u_* turbulent velocity standard deviations for the solid and porous configurations, respectively, where $\sigma_s = (\overline{s'^2})^{1/2}$, and s is an arbitrary flow variable. The zone of most intense velocity variances is situated

near the interface between the flow inside the gap and aloft. Within this zone, the production of turbulent kinetic energy scales with $\partial\overline{U}/\partial z$, which is largest at this interface for both flow configurations. For the porous boundary, σ_u/u_* and σ_w/u_* increase to values as high as 2.2 and 1.6, respectively, around this interface. These maximum values of σ_u/u_* and σ_w/u_* for the porous case are larger than their counterparts for the solid case (i.e. turbulence is more energetic). However, it should be noted that the increases in σ_u/u_* and σ_w/u_* from their undisturbed upstream state are larger for the solid case by comparison to the porous case, which suggests more turbulent kinetic energy was produced by the sharp corner. What is perhaps more significant here is the impact of the boundary cover on the spatial persistence of these large σ_u/u_* and σ_w/u_* downstream of GF_D. For the porous boundary case, the persistence of a large σ_u/u_* and σ_w/u_* downstream of GF_D is far more significant when compared to the solid boundary case. In part, this persistence for the porous boundary case is analogous to flows into forest edges initiated from a clearing as noted elsewhere (Belcher et al. 2003; Dupont and Brunet 2008; Cassiani et al. 2008). As with the velocity variances, the zone of large normalized turbulent shear stress $\overline{u'w'}$ exists at the interface just above and just below the gap with values reaching up to twice the values of the undisturbed wall stress upstream. Moreover, as with the velocity variances, the zone of large $\overline{u'w'}$ is wider for the porous case when compared to the solid boundary case. The implications of these spatial patterns on the advective and turbulent transport terms in the mean longitudinal and vertical momentum balances are considered next.

3.3 Advective and Turbulent Transport

Away from boundaries and at high Reynolds numbers, the mean longitudinal and vertical momentum balances for a stationary flow in the absence of any density gradients are given as

$$\overline{U}\frac{\partial\overline{U}}{\partial x}+\overline{W}\frac{\partial\overline{U}}{\partial z}=-\frac{1}{\rho_w}\frac{\partial\overline{P}}{\partial x}-\frac{\partial\overline{u'w'}}{\partial z}-\frac{\partial\overline{u'u'}}{\partial x}, \tag{1}$$

$$\overline{U}\frac{\partial\overline{W}}{\partial x}+\overline{W}\frac{\partial\overline{W}}{\partial z}=-\frac{1}{\rho_w}\frac{\partial\overline{P}}{\partial z}-\frac{\partial\overline{u'w'}}{\partial x}-\frac{\partial\overline{w'w'}}{\partial z}, \tag{2}$$

where ρ_w is the mean density of water, and the mean pressure ($\overline{P}$) term here is assumed to be a perturbation from a hydrostatic reference state. How the boundary configurations affect the individual advective and turbulent transport terms in both mean momentum budgets is explored in Figs. 7 and 8. For the mean longitudinal momentum balance, the spatial variations in the vertical advective ($\overline{W}\partial\overline{U}/\partial z$), longitudinal advective ($\overline{U}\partial\overline{U}/\partial x$), and turbulent transport ($\partial\overline{u'w'}/\partial z+\partial\overline{u'u'}/\partial x$) terms are first discussed. The vertical advective term is most significant in magnitude within the gap, where large negative values are expected based on $\overline{W}$ and noted in the upstream vicinity of GF_D. The effect of the boundary on $\overline{W}\partial\overline{U}/\partial z$ is most significant downstream from GF_D. In this region, a positive $\overline{W}\partial\overline{U}/\partial z$ is set-up for both boundary configurations though the porous case appears more spatially expansive when compared to its solid counterpart. For the horizontal advective term, its spatial variations are generally 'in-phase' with the vertical advective term inside the gap. In other regions of the flow domain, the horizontal advective term exhibits a more complex spatial pattern and appears more sensitive to the boundary cover when compared to its vertical advective counterpart. For the porous case and at GF_U, the horizontal advective term is positive and large, while at GF_D the horizontal advective term switches sign but retains the large amplitude. At the downstream corner end of the GF_D, the horizontal advective term is positive. For the

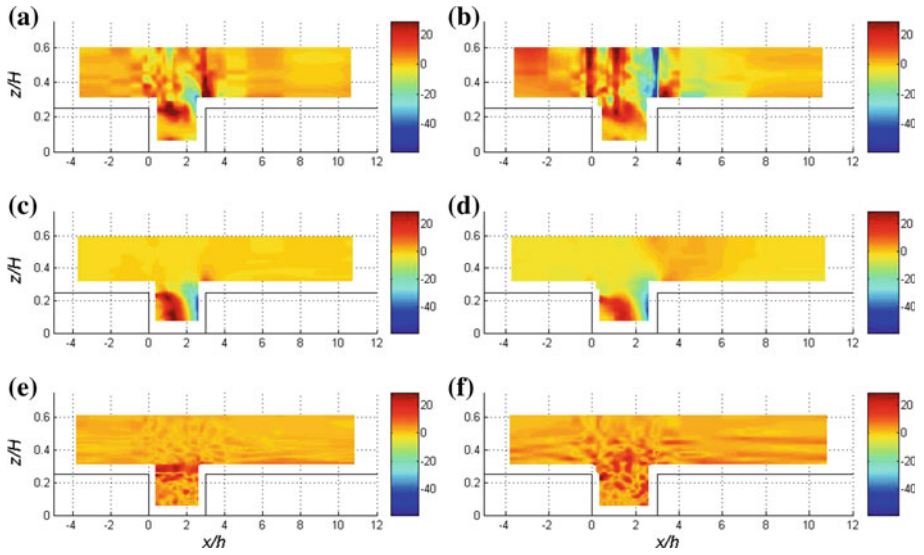

Fig. 7 Spatial variation of the advective and turbulent transport terms for the mean longitudinal momentum balance for the solid (*left*) and porous (*right*) cases. **a, b** $\overline{U}\frac{\partial \overline{U}}{\partial x}$ $(h/(u_*)^2)$, **c, d** $\overline{W}\frac{\partial \overline{U}}{\partial z}$ $(h/(u_*)^2)$, **e, f** $\left(\frac{\partial \overline{u'w'}}{\partial z} + \frac{\partial \overline{u'u'}}{\partial x}\right)(h/(u_*)^2)$

turbulent transport terms, their values are most significant inside the gap for both boundary configurations, though their magnitude is smaller for the porous configuration when compared to their solid counterparts. The spatial variations in the vertical advective $(\overline{W}\partial\overline{W}/\partial z)$, longitudinal advective $(\overline{U}\partial\overline{W}/\partial x)$, and turbulent transport $(\partial\overline{u'w'}/\partial x + \partial\overline{w'w'}/\partial z)$ terms are discussed here for the vertical momentum balance. The vertical advective term appears to be small and can be ignored except inside the gap. This finding also appears to be insensitive to whether the boundary configuration is solid or porous. The horizontal advective terms are significant within and above the gap and sensitive to the boundary configuration. The turbulent transport terms appear to be significant within the gap and immediately above it. For the solid configuration, these transport terms are large at the interface between the flow inside and above the gap. For the porous configuration, this interface of intense turbulent transport is displaced deeper into the gap. When taken together, these results suggest that the flows adjacent and inside gaps are not amenable to simplified theoretical treatment as virtually all the terms in the mean momentum balance (vertical and horizontal) appear significant.

3.4 Sweeps, Ejections and Momentum Transport Efficiency

In this section, the relative importance of ejections and sweeps and the relative transport efficiency of direct and indirect fluxes that quantify the transport of momentum (locally) are discussed. In keeping with standard convention, when $\overline{u'w'} < 0$ the terms 'direct', 'indirect', 'ejections', and 'sweeps' are defined via quadrant analysis formed by the plane whose abscissa is u' and whose ordinate is w' (Antonia 1981). The direct and indirect fluxes define events whose $w'u' < 0$ (quadrants 2 and 4) and $w'u' > 0$ (quadrants 1 and 3), respectively. The terms sweeps and ejections refer to events situated in quadrants 4 ($u' > 0$ and $w' < 0$) and 2 ($u' < 0$ and $w' > 0$), respectively, of the $w' - u'$ cartesian plane. There are instances

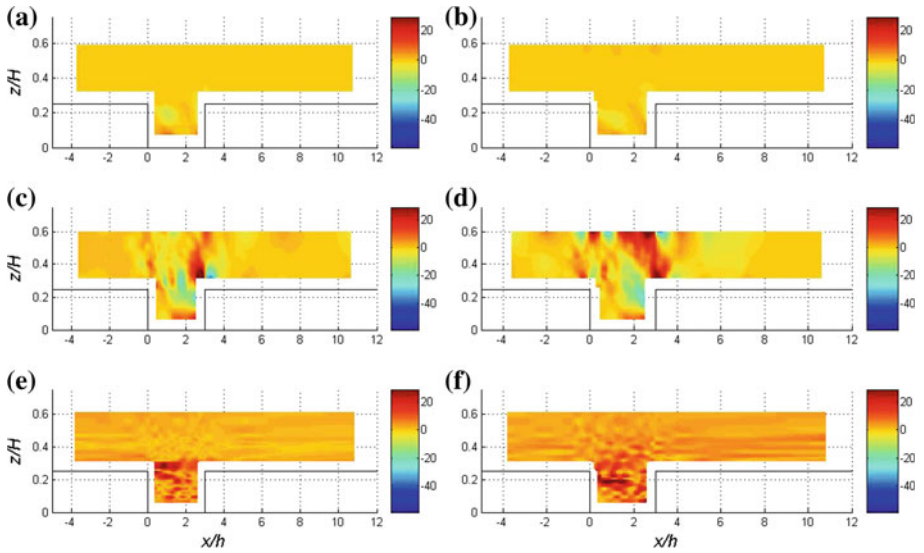

Fig. 8 Spatial variation of the advective and turbulent transport terms for the mean vertical momentum balance for the solid (*left*) and porous (*right*) cases. **a, b** $\overline{W}\frac{\partial \overline{W}}{\partial z}$ $(h/(u_*)^2)$, **c, d** $\overline{U}\frac{\partial \overline{W}}{\partial x}$ $(h/(u_*)^2)$, **e, f** $\left(\frac{\partial \overline{u'w'}}{\partial x} + \frac{\partial \overline{w'w'}}{\partial z}\right)(h/(u_*)^2)$

where $\overline{u'w'} > 0$ occurs in a small and restricted region near the bottom corner of GF_D. For this region, the quadrants affiliated with these definitions reverse. However, for much of the flow domain, $\overline{u'w'} < 0$, and the standard quadrant convention for defining direct, indirect, sweeps, and ejections, is employed unless otherwise stated. The relative fraction of $\overline{u'w'}$ transported by ejections and sweeps is given as (Raupach 1981)

$$\Delta S_0 = \frac{(\overline{u'w'})_4 - (\overline{u'w'})_2}{\overline{u'w'}}, \tag{3}$$

where $\left(\overline{u'w'}\right)_4$ and $\left(\overline{u'w'}_2\right)$ are momentum flux contributions originating from quadrants 4 (sweeps) and 2 (ejections), respectively. Here, $\Delta S_0 > 0$ signifies the dominant role of sweeps, while $\Delta S_0 < 0$ signifies the dominant role of ejections in momentum transport. The results in Fig. 9a, b show that much of the $\overline{u'w'}$ outside the gap is dominated by ejection for both boundary configurations; however, $\overline{u'w'}$ inside the gap is primarily dominated by sweeps. The bottom corner region of GF_U inside the gap is dominated by ejections. For the porous boundary case, the $\Delta S_0 > 0$ within the gap is roughly co-located with the zone of the free-shear interface earlier discussed. For the solid boundary case, the zone of intense sweeps appears less well defined within the gap except close to the ground. However, for both surfaces, the relative importance of ejections and sweeps follows the overall mean circulation pattern inside the gap. In the adjustment region immediately downstream from GF_D, ejections dominate the $\overline{u'w'}$ transport for a horizontal distance roughly commensurate with H in the region close to the ground or porous surface for both boundaries. The transport efficiency of direct and indirect fluxes can be defined as the ratio of the net flux to the direct flux and is given as(Wyngaard and Moeng 1992; Li and Bou-Zeid 2004)

$$T_e = \frac{Direct\ Flux + Indirect\ Flux}{Direct\ Flux} = 1 + \frac{\left[(\overline{u'w'})_1 + (\overline{u'w'})_3\right]}{\left[(\overline{u'w'})_4 + (\overline{u'w'})_2\right]}. \tag{4}$$

If all the $\overline{u'w'}$ originates from the direct flux component, then $T_e = 1$, and if the direct and indirect fluxes contribute equally, then $T_e = 0$. Figure 9c, d shows the spatial variation of T_e for the solid and porous configurations. As with the ΔS_o, the highest T_e is situated in the free-shear layer area within the gap, and the smallest T_e is situated in the bottom lower corner of GF_D. The high T_e associated with this free-shear layer appears to 'fill' more of the gap space for the porous boundary when compared to its solid boundary counterpart. With regards to modelling ΔS_o and T_e, it is instructive to ask how detailed the joint probability density functions (pdf_{uw}) between u' and w' must be resolved before all the spatial patterns in Fig. 9 can be reproduced. A similar (though not identical) problem has been considered in a number of turbulent flows (Frenkiel and Klebanoff 1967; Durst et al. 1992) in which the pdf_{uw} was expanded via Gram-Charier cumulants and the number of cumulants that must be retained to describe the statistical properties of ΔS_o and T_e was evaluated. A logical starting point to address this problem is the relationship between ΔS_0 and third-order cumulants (or CEM) given as (Nakagawa and Nezu 1977; Raupach 1981),

$$\Delta S_0 = \frac{1+\rho}{\rho\sqrt{2\pi}}\left(\frac{2C_1}{(1+\rho)^2} + \frac{C_2}{1+\rho}\right), \tag{5}$$

where $\rho = \overline{u'w'}/(\sigma_u\sigma_w)$ is the correlation coefficient between u' and w', C_1 and C_2 are given as

$$C_1 = (1+\rho)\left[\frac{1}{6}(M_{03} - M_{30}) + \frac{1}{2}(M_{21} - M_{12})\right], \tag{6}$$

$$C_2 = -\left[\frac{1}{6}(2-\rho)(M_{03} - M_{30}) + \frac{1}{2}(M_{21} - M_{12})\right], \tag{7}$$

where M_{03}, M_{30}, M_{21} and M_{12} are the third- (or mixed) order moments of the rescaled velocity components given as

$$M_{ij} = \overline{\left(\frac{u'}{\sigma_u}\right)^i \left(\frac{w'}{\sigma_w}\right)^j}. \tag{8}$$

An 'incomplete' cumulant expansion (ICEM) (i.e. some terms in a third-order cumulant expansion are discarded) can also be derived by neglecting contributions from M_{03} and M_{30}. This approximation was shown to be reasonably accurate in other studies (Katul et al. 1997; Fer et al. 2004; Poggi et al. 2004; Cava et al. 2006; Katul et al. 2006). With this truncation, the main contributions to ΔS_o originate from M_{21} and M_{12} and the third-order CEM simplifies to:

$$\Delta S_o(ICEM) = \frac{1}{2\sqrt{2\pi}\,\rho}(M_{21} - M_{12}). \tag{9}$$

A comparison between ΔS_o inferred from quadrant analysis, the CEM, and ICEM for both solid and porous boundaries is shown in Fig. 10a, b. Despite the large inhomogeneity in the flow, the ability of the ICEM to reproduce measured ΔS_o is suggestive that the mixed moments M_{12} and M_{21} dictate the behaviour of ΔS_o far more than the two velocity skewnesses. These two moments are directly linked to the flux transport terms ($\overline{w'w'u'}$ and $\overline{w'u'u'}$) in the turbulent kinetic energy budget as discussed elsewhere (Katul et al. 1997;

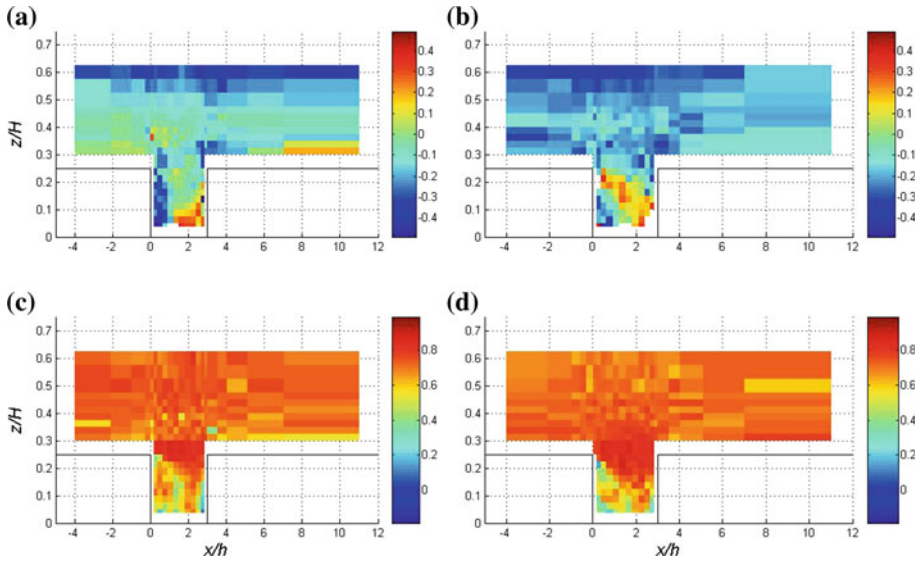

Fig. 9 The spatial variation of ΔS_0 (**a, b**) and T_e spatial variation (**c, d**) for the solid (*left*) and porous (*right*) configurations

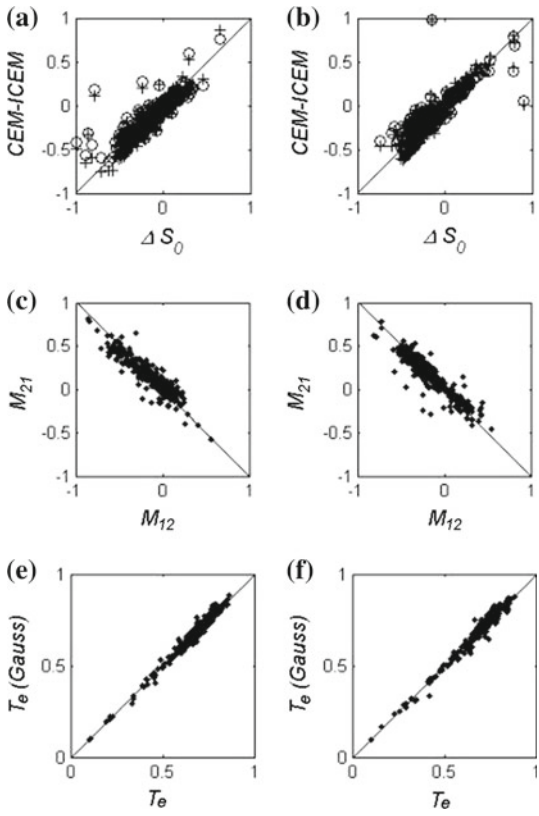

Fig. 10 Comparison between modelled ΔS_0 from CEM (*open circle*) and ICEM (*plus*) against ΔS_0 from quadrant analysis (**a, b**), comparison between measured M_{12} and measured M_{21} for all measurement locations in the flow domain (the *regression lines* are also shown) (**c, d**) and comparison between measured and modelled T_e using a Gaussian distribution (**e, f**) for the solid (*left panels*) and porous (*right panels*) boundaries

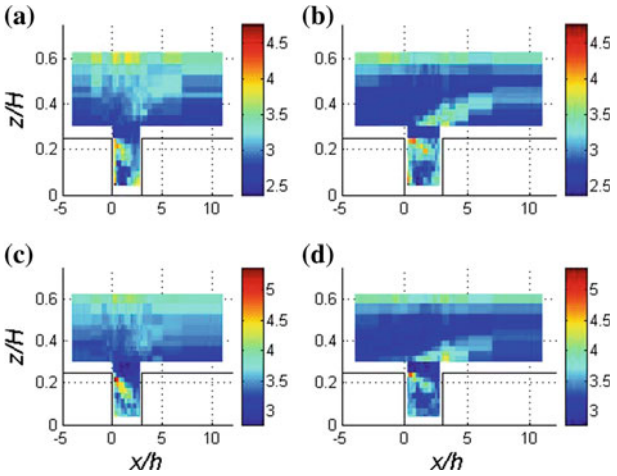

Fig. 11 Spatial variation of the longitudinal velocity (**a, b**) and vertical velocity (**c, d**) flatness factor (FF) for the solid (*left*) and porous (*right*) cases

Poggi et al. 2004; Cava et al. 2006). Moreover, as discussed in a number of studies (Raupach 1981), M_{12} and M_{21} are usually inversely related to each other. Wind-tunnel studies have shown that $M_{12} \approx -M_{21}$ in rough-wall boundary layers and across a wide range of surface roughness values (Raupach 1981). On the other hand, canopy flow experiments suggest that $M_{12} \approx -0.6M_{21}$ for measurements within the canopy and near the canopy top as well as across a wide range of atmospheric stability conditions (Cava et al. 2006). For the dataset here, this relationship is explored in Fig. 10 for both boundary configurations. From this figure, $M_{12} \approx -0.82M_{21}$ describes well the data for both solid and porous boundaries even when combining all measurement locations. Hence, this result demonstrates that only one of the two flux transport terms is actually needed to describe ΔS_o when using the ICEM. Next, the simplest representation for T_e, which is derived from a joint Gaussian distribution assumption for P_{uw}, is discussed. For a Gaussian P_{uw}, the transport efficiency is given as (Wyngaard and Moeng 1992)

$$T_e = \frac{2\pi\rho}{2\sqrt{1-\rho^2} + \pi\rho + 2\rho sin^{-1}(\rho)}, \tag{10}$$

so that T_e can be described entirely from ρ for a Gaussian P_{uw}. Figure 10e, f compare the measured T_e from quadrant analysis and the modelled T_e from Eq. 10 for both configurations. The good agreement between measured and modelled T_e for solid and porous configurations is rather surprising given the severe inhomogeneity in the flow. These results indicate that, despite the large inhomogeneity in the flow and differences in boundary conditions, much of the properties of the ejections and sweeps can be described by simplified representations of P_{uw} that resolve one of the two mixed moments.

To further explore the non-Gaussianity in the velocity field for both configurations, the flatness factor FF (or kurtosis) is computed and shown in Fig. 11. For a Gaussian flow field, $FF = 3$. Because FF is sensitive to large turbulent excursions from the mean, its value is dominated by the so-called active or energetic phases of the flow variable and hence is often used to characterize their intermittency (Batchelor and Townsend 1949; Sandborn 1959). Figure 11 demonstrates that $FF > 3$ at the upstream corner for both solid and porous

configurations. For the downstream end of the cavity, FF again increases beyond 3 when the flow encounters the corner of the porous boundary though not as much increases in FF are evident for the solid configuration. This enhanced FF zone over the porous configuration roughly coincides with the zone of intense turbulence already highlighted in Fig. 1. FF is also enhanced near the top of the boundary layer given the intermittent nature of the turbulence near the free water surface. Across the entire flow domain, FF for the vertical velocity generally exceeded those of the longitudinal velocity, but the range in FF was between 2.5 and 4.5. Such a range in FF is not too far from Gaussian behaviour, again suggesting that a third-order CEM may suffice to describe the tails of P_{uw} and thus the ejection-sweep properties.

4 Summary and Conclusions

How the porosity of the boundary controls the flow within and above a regular gap was explored using DLV and LDA experiments. The DLV experiments showed that for a ratio of gap-length to gap-depth values of around 3, the free-shear layer interface spawned at the upstream gap corner intersects the downstream gap face just prior to the formation of a re-attachment point. Because the dynamics of this particular configuration are not dominated by complex re-attachment and re-equilibration zones, it was selected for exploring the mean and turbulent flow for a porous and a solid boundary surrounding a gap. The LDA measurements were used to evaluate the effects of the porous versus solid boundary on, (i) bulk flow properties including the mean vorticity within and adjacent to the gaps, (ii) second-order statistics such as the standard deviations and turbulent stresses, (iii) the relative importance of advective to turbulent stress terms across various regions within and above the gaps, and (iv) the local imbalance between ejections and sweeps and momentum transport efficiencies of updrafts and downdrafts. The LDA data were normalized with the boundary-layer height, the gap height and the friction velocity at an upstream distance not significantly disturbed by the gap. For the solid configuration, the $\overline{U}$ component above the gap appears to be insensitive to the presence of the gap. In contrast, for the porous configuration, the $\overline{U}$ magnitude increases in the upper layers situated above the gap. Moreover, for both boundary configurations, the measurements inside the gap show a rapid decrease in $\overline{U}$. Commencing at the upstream corner of the gap, $\overline{U}$, normalized with the undisturbed friction velocity, is about 3, resembling a free-shear mixing layer. This upstream corner is also shown to be responsible for spawning a large mean vorticity, which is more intense for the solid boundary. The LDA measurements demonstrated that the horizontal advective terms are most significant above the gap for both boundary configurations. Turbulent transport terms are important only inside the gap, where the vertical advective term for the longitudinal momentum balance dominates over its longitudinal counterpart. Another important conclusion here is the possibility of describing the relative importance of ejections and sweeps to momentum transfer by using only one of the two flux transport terms. Moreover, it is demonstrated that the transport efficiency can be described entirely by a joint Gaussian distribution. These last two conclusions are surprising given the large inhomogeneity and the non-Gaussianity in the flow statistics detected by the flatness factor—but they are suggestive that few cumulants connected to the flux transport terms can describe P_{uw} for the purposes of modeling the ejection-sweep statistical properties.

Acknowledgments G. G. Katul acknowledges support from the U.S. Department of Energy through the Office of Biological and Environmental Research (BER) Terrestrial Ecosystem Science (TES) program (DE-SC000697), the U.S. National Science Foundation (NSF-AGS-1102227, NSF-CBET-103347,

NSF-EAR-10-13339), the U.S. Department of Agriculture (2011-67003-30222), and the Fulbright-Italy distinguished scholars program. Poggi acknowledges support from the Commission of the European Communities (WARECALC) program (PIRSES-GA-2008-230845).

Appendix: Post Processing of the Velocity Data

Because the LDA velocity measurements are used to evaluate the mean vorticity and the advective terms in the mean longitudinal and vertical momentum balances, the estimation of the spatial gradients must be discussed given the unavoidable measurement errors. While various approaches are available to interpolate and compute spatial gradients for noisy data, the approach followed here is intended to correct the time-averaged $\overline{U}$ and $\overline{W}$ to ensure that the mean continuity equation, given as

$$\frac{\partial \overline{U}}{\partial x} = -\frac{\partial \overline{W}}{\partial z} \tag{11}$$

is closely satisfied and any departure from it is minimized. In this approach, a Lagrange multiplier method that minimizes the velocity corrections $(\overline{U} - \overline{U}_0)^2$ and $(\overline{W} - \overline{W}_0)^2$ is used and is given as

$$\int\int_{\Omega} \alpha_1^2(\overline{U} - \overline{U}_0)^2 + \alpha_2^2(\overline{W} - \overline{W}_0)^2 dxdz = \int\int_{\Omega} \lambda \left(\frac{\partial \overline{U}}{\partial x} + \frac{\partial \overline{W}}{\partial z} \right) dxdz. \tag{12}$$

Here, the $\overline{U}_0$, $\overline{W}_0$ are the acquired mean velocity components that need not satisfy the mean continuity equation. The mean velocities $\overline{U}$ and $\overline{W}$ are the error-free velocities that satisfy the mean continuity equation. The difference $(\overline{U} - \overline{U}_0)$ and $(\overline{W} - \overline{W}_0)$ are the corrections to be minimized so as to find $\overline{U}$ and $\overline{W}$ as close as possible to the acquired data. The scheme here is aimed at applying as small as possible a correction to the LDA measured velocity so that they optimally satisfy the mean continuity equation. The terms α_1^2, α_2^2 are Gaussian precision moduli that consider particular flow conditions in which a component is more important than the other one. The parameter α governs the adjustment between the two velocity components. In these experiments, as is the case for neutral atmospheric conditions studied elsewhere, it is possible to assume both coefficients are equal to unity. In stable atmospheric flow conditions, it is common to assume that α_2^2 exceeds α_1^2 and vice versa for unstable condition. Minimizing Eq. 12 is equivalent to minimizing the correction needed to be added to each velocity component to ensure the mean continuity equation is satisfied. The solution of this minimization problem is equivalent to solving the Euler-Lagrange set of equations comprised of the elliptic system, given by

$$\frac{\partial^2 \lambda}{\partial x^2} + \left(\frac{\alpha_1}{\alpha_2} \right)^2 \frac{\partial^2 \lambda}{\partial z^2} = -2\alpha_1^2 \left(\frac{\partial \overline{U}_0}{\partial x} + \frac{\partial \overline{W}_0}{\partial z} \right) \tag{13}$$

where the corrections derived from the solution to Eq. 13 are given as

$$\overline{U} = \overline{U}_0 + \frac{1}{2\alpha_1^2} \frac{\partial \lambda}{\partial x}; \quad \overline{W} = \overline{W}_0 + \frac{1}{2\alpha_2^2} \frac{\partial \lambda}{\partial z}. \tag{14}$$

These corrections, as represented in Eq. 14, are applied to the mean velocity components prior to computing spatial gradients. In Fig. 12, the corrected velocity gradients show that the mean continuity equation is reasonably well satisfied for all points in the flow domain.

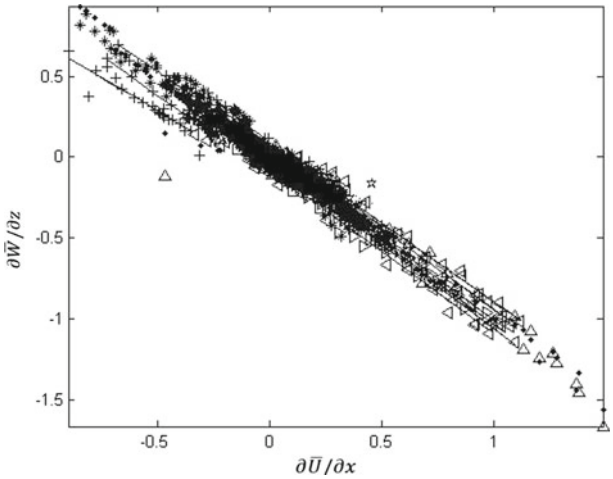

Fig. 12 The mean continuity equation terms $\partial \overline{U}/\partial x$ against $\partial \overline{W}/\partial z$ after the proposed post-processing and corrections

References

Antonia RA (1981) Conditional sampling in turbulence measurements. Annu Rev Fluid Mech 13:131–156
Albertson JD, Parlange MB (1999) Surface length scales and shear stress: implications for land–atmosphere interaction over complex terrain. Water Resour Res 35:2121–2132
Ashcroft G, Zhang X (2005) Vortical structures over rectangular cavities at low speed. Phys Fluids 17:015104-1–015104-8
Batchelor GK, Townsend AA (1949) The nature of turbulent motion at large wavenumbers. Proc R Soc A 199:238–255
Belcher SE, Jerram N, Hunt JCR (2003) Adjustment of a turbulent boundary layer to a canopy of roughness elements. J Fluid Mech 488:369–398
Cassiani M, Katul GG, Albertson JD (2008) The effects of canopy leaf area index on airflow across forest edges: large-eddy simulation and analytical results. Boundary-Layer Meteorol 126:433–460
Cava D, Katul GG, Scremieri A, Poggi D, Cescatti A, Giostra U (2006) Buoyancy and the sensible heat flux budget within a dense canopy. Boundary-Layer Meteorol 118:217–240
Detto M, Katul GG, Siqueira MB, Juang JY, Stoy P (2008) The structure of turbulence near a tall forest edge: the backward facing step flow analogy revisited. Ecol Appl 18:1420–1435
Dupont S, Brunet Y (2008) Edge flow and canopy structure: a large-eddy simulation study. Boundary-Layer Meteorol 126:51–71
Durst F, Jovanovic J, Johansson TG (1992) On the statistical proprieties of truncated Gram-Charlier series expansions in turbulent wall-bounded flows. Phys Fluids A 4(1):118–126
Fer I, McPhee MG, Sirevaag A (2004) Conditional statistics of the Reynolds Stress in the under-ice boundary layer. Geophys Res Lett 31:2004GL020475
Finnigan J (2000) Turbulence in plant canopies. Annu Rev Fluid Mech 32:519–571
Frenkiel F, Klebanoff P (1967) Higher order correlations in a turbulent field. Phys Fluids 10:507–522
Irvine MR, Gardiner BA, Hill MK (1997) The evolution of turbulence across a forest edge. Boundary-Layer Meteorol 84:467–496
Katul GG, Hsieh CI, Kuhn G, Ellsworth D, Nie D (1997) The turbulent eddy motion at the forest–atmosphere interface. J Geophys Res 102:13409–13421
Katul GG, Geron CD, Hsieh CI, Vidakovic B, Guenther AB (1998) Active turbulence and scalar transport near the land–atmosphere interface. J Appl Meteorol 37:1533–1546
Katul GG, Poggi D, Cava D, Finnigan D (2006) The relative importance of ejections and sweeps to momentum transfer in the atmospheric boundary layer. Boundary-Layer Meteorol 120:367–375
Klaassen W (1992) Average fluxes from heterogeneous vegetated regions. Boundary-Layer Meteorol 58:329–354

Laurence W (2004) Forest climate interactions in fragmented tropical landscapes. Philos Trans R Soc Lond 359:345–352
Li D, Bou-Zeid E (2011) Stability effects on turbulent coherent structures and transport efficiency in the atmospheric surface layer. Boundary-Layer Meteorol 140(2):243–262
Manes C., Poggi D., Ridolfi L. (2011) Turbulent boundary layers over permeable walls: scaling and near-wall structure. J Fluid Mech 687:141–170
Nakagawa H, Nezu I (1977) Prediction of the Reynolds stress from bursting events in open-channel flows. J Fluid Mech 80:99–128
Poggi D, Porporato A, Ridolfi L (2002) An experimental contribution to near-wall measurements by means of a special laser Doppler anemometry technique. Exp Fluids 32:366–375
Poggi D, Katul GG, Albertson JD (2004) Momentum transfer and turbulent kinetic energy budgets within a dense model canopy. Boundary-Layer Meteorol 111:589–614
Poggi D, Katul GG, Albertson JD (2006) Scalar dispersion within a model canopy: measurements and three-dimensional Lagrangian models. Adv Water Resour 29:326–335
Poggi D, Katul GG, Vidakovic B (2011) The role of wake production on the scaling laws of scalar concentration fluctuation spectra inside dense canopies. Boundary-Layer Meteorol 139:83–95
Pope SB (2000) Turbulent flows. Cambridge University Press, UK, 771 pp
Raupach MR (1981) Conditional statistics of Reynolds stress in rough-wall and smooth-wall turbulent boundary layers. J Fluid Mech 108:363–382
Raupach MR, Finnigan JJ, Brunet Y (1996) Coherent eddies and turbulence in vegetation canopies: the mixing layer analogy. Boundary-Layer Meteorol 78:351–382
Sandborn VA (1959) Measurements of intermittency of turbulent motion in a boundary layer. J Fluid Mech 6:221–240
Schlegel F, Stiller J, Bienert A, Maas HG, Queck R, Bernhofer C (2012) Large-eddy simulation of inhomogeneous canopy flows using high resolution terrestrial laser scanning data. Boundary-Layer Meteorol 142:223–243
Seraphin A, Guyenne P (2008) A flume experiment on the adjustment of the mean and turbulent statistics to a transition from short to tall sparse canopies. Boundary-Layer Meteorol 129:47–64
Simpson RL (1989) Turbulent boundary layer separation. Annu Rev Fluid Mech 21:3808–3818
Spazzini PG, Iuso G, Onorato M, Zurlo N, Di Cicca GM (2001) Unsteady behavior of back-facing step flow. Exp Fluids 30:551–561
Thomas KF, Wilson JD (1999) Wind and remnant tree sway in forest cutblocks. I. Measured winds in experimental cutblocks. Agric For Meteorol 93:229–242
Veen WL, Klaassen W, Kruijt B, Hutjes RWA (1996) Forest edges and the soil–vegetation–atmosphere interaction at the landscape scale: the state of affairs. Prog Phys Geogr 20:292–310
Wyngaard JC, Moeng CH (1992) Parameterizing turbulent diffusion through the joint probability density. Boundary-Layer Meteorol 60:1–13
Yang B, Raupach MR, Shaw RH, Tha K, Paw U, Morse AP (2006a) Large-eddy simulation of turbulent flow across a forest edge. Part I: flow statistics. Boundary-Layer Meteorol 120:377–412
Yang B, Morse AP, Shaw RH, Tha K, Paw U (2006b) Large-eddy simulation of turbulent flow across a forest edge. Part II: momentum and turbulent kinetic energy budgets. Boundary-Layer Meteorol 121:433–457